# Friction anisotropy and associated surface deformation mechanisms in heterogeneous copper/bronze laminates

Qicheng Zhang [a], Yong Li [a], Fei Liang [a], Zhongchen Zhou [a], Yusheng Li [a], Julia Rau [b,c], Christian Greiner [b,c], Yonghao Zhao [a], Yuntian Zhu [d], Xiang Chen [a,*]

[a] Nano and Heterogeneous Materials Center, School of Materials Science and Engineering, Nanjing University of Science and Technology, Nanjing 210094, China
[b] Institute for Applied Materials (IAM), Karlsruhe Institute of Technology (KIT), Karlsruhe 76131, Germany
[c] IAM-ZM MicroTribology Center μTC, Karlsruhe, Germany
[d] Department of Materials Science and Engineering, City University of Hong Kong, Hong Kong, China

*Keywords:*
Heterogeneous laminates
Friction anisotropy
Chemical mixing
Strain delocalization
Interfacial plasticity

A B S T R A C T

Heterogeneous laminates have demonstrated an extraordinary combination of strength and ductility. However, their response to tribological loading remains elusive. Here, a series of bulk heterogeneous Cu/CuZn laminates with layer spacings from 20 to 200 μm were prepared, to systematically investigate the role of layer spacing and sliding direction on friction and wear. We find that below a critical spacing value or above a tribological stress threshold, the friction coefficient and wear rate during sliding perpendicular to the laminate interface are much lower than the parallel one. When sliding parallel to the interfaces, the formation of a brittle nanostructured tribolayer dominates in the CuZn layers for all sliding cycles. While sliding perpendicular to the interfaces in the early stage, many deformation twins and dislocations form close to the interfaces in the CuZn layer, producing strain gradients and thus alleviating the strain localization. In the late stage of the sliding contact, friction-induced chemical mixing perpendicular to the interfaces is significantly stimulated below the critical layer spacing, mitigating the formation of a delaminating tribolayer. The observed friction anisotropy is intimately related to interface-induced strain delocalization, providing guidelines in designing the heterogeneous laminates with outstanding tribological properties.

## 1. Introduction

Controlling friction in materials tribology, particularly for metallic materials during dry sliding, has been a long-standing challenge. First, polycrystalline metals display high steady-state coefficients of friction (COFs), leaving limited room for modifications of chemical compositions [1]. The main cause is deformation-induced surface roughening and unavoidable strain localization in contacts. Second, alterations of the grain size to the nanoscale are insufficient to mitigate friction and wear under high tribological loading, although a substantial difference in hardness exists [2,3]. This stems from the low strain capability of nanograins and the formation of a delaminating nanograined tribolayer beneath the surface. The frictional force was intimately related to plastic deformation in the contact surface and subsurface layer, and friction reductions were only observed in metals with stable nanograins under very mild sliding conditions [4–6].

The motivation to modulate friction has triggered numerous interests through surface morphology modification in the past decades. As a typical example, surface texturing [7–9] was demonstrated to be potent and effective in not only optimizing the tribological behavior, but also providing friction anisotropy [10,11]. The texturing elements mainly consist of dimples [12,13] and grooves [14,15] with dimensions ranging from several tens to hundreds of microns. For grooves, the friction anisotropy was frequently reported to be dependent on their width, depth and spacing. For instance, an optimal groove spacing of 75 μm was found to excite the highest friction anisotropy and provide better tribological properties when sliding perpendicular to the grooves under dry conditions for surface textured 304 L stainless steel [16]. The postulated mechanisms for friction reduction include the trapping and storage of wear debris or lubricants, reduction of contact area, and improvement in heat transfer [8]. However, a lack of long-term sustainability greatly limits their applications when the morphological textures are filled with wear debris or entirely removed.

In recent years, efforts have shifted to the issue of mitigating friction

* Corresponding author.
*E-mail address:* xiang.chen@njust.edu.cn (X. Chen).

and wear by introducing a gradient nano-grained (GNG) structure [17–23], i.e. a spatial gradient in grain size increasing from tens of nanometers at the surface to micrometers in the bulk. Such a heterogeneous GNG structure enables a remarkable reduction of COFs and wear rates by one order of magnitude in Cu and Cu alloys, due to the suppression of friction-induced strain localization [20–22]. In a broad sense, heterogeneous materials exhibit characteristics of diverse microstructures over a wide range of length scales, including the GNG structure mentioned above, as well as heterogeneous lamella structure [24,25], laminate structure [26–29], multi-modal grain structure [30] and harmonic structure [31,32], to name a few examples. These heterogeneous materials share one common feature: soft domains are constrained by hard domains in an intelligently designed fashion. For instance, heterogeneous bulk Cu/CuZn laminates with different coarse lamellae spacings (3.7–125 μm) were reported to display an unparalleled combination of high strength and ductility [27]. Regarding their fundamental deformation mechanisms, strain partitioning occurs among the Cu/CuZn interfaces after yielding, bringing about back stresses in the soft Cu domains and forward stresses in the hard CuZn ones, which is known as hetero-deformation induced (HDI) hardening [33]. It was further pointed out that there exists an interface affected zone with strain gradients, and the design guideline to attain the maximum HDI hardening effect is to render the interface affected zone comparable to half of the lamellar spacing (15 μm) [27]. Although such a heterogeneous laminate is supposed to bring about strain delocalization under monotonic deformation modes, the question arises to whether it is effective in mitigating friction-induced strain localization.

Going back to the literature, the tribological behaviors of nanoscale metallic multilayers films (lamellae spacing less than 100 nm) have been extensively investigated, such as Au/Ni [34], Cu/Ni [35], Cu/Au [36,37], Cu/Nb [38] and NbMoWTa/Ag [39], etc. For Au/Ni multilayers, the COF reduces with decreasing layer spacing from 100 to 10 nm due to transitions from dislocation-mediated to grain boundary-mediated deformation in the subsurface layer [34]. More recently, single nanoscratch tests were carried out on immiscible Cu/Nb nanolaminates with a diamond tip (40 nm in radius) moving perpendicular to the laminate interfaces [38]. A transition from intra-layer dislocations slipping to dislocations slip across the interface occurs when the layer spacing is less than a critical size (~8 nm), boosting the interfacial plasticity and thus forcing chemical mixing. Moreover, molecular dynamics simulations indicate that the interfaces play roles in strain delocalization or deformation coordination during tensile or friction deformation of heterogeneous metallic laminates [40,41]. Note that macroscopic friction tests can only be carried out parallel to the interface planes instead of perpendicular to the interfaces, basically limited to the thickness of multilayers films [42,43]. Consequently, the effect of the lamellae spacing and the role of interfaces on friction and wear remain elusive for bulk laminates.

In this paper, a series of bulk heterogeneous Cu/CuZn laminates with layer spacing from 20 to 200 μm were prepared. These bulk laminates serve as ideal model materials to systematically investigate the influence of layer spacing on the tribological properties, and to examine the friction and wear anisotropy under different sliding directions for the first time. By tracking the surface and subsurface structural and chemical changes, the prevailing friction, wear and associated surface deformation mechanisms in heterogeneous copper/bronze laminates are delineated.

## 2. Materials and methods

### 2.1. Sample preparation

The Cu/CuZn bulk laminates were fabricated through diffusion welding and cold rolling, as illustrated in Fig. 1a. Commercial pure copper (99.9 wt%) and bronze (Cu-32 wt% Zn) sheets were utilized as the raw materials (Tengyu Metals Co., China). The sheets were

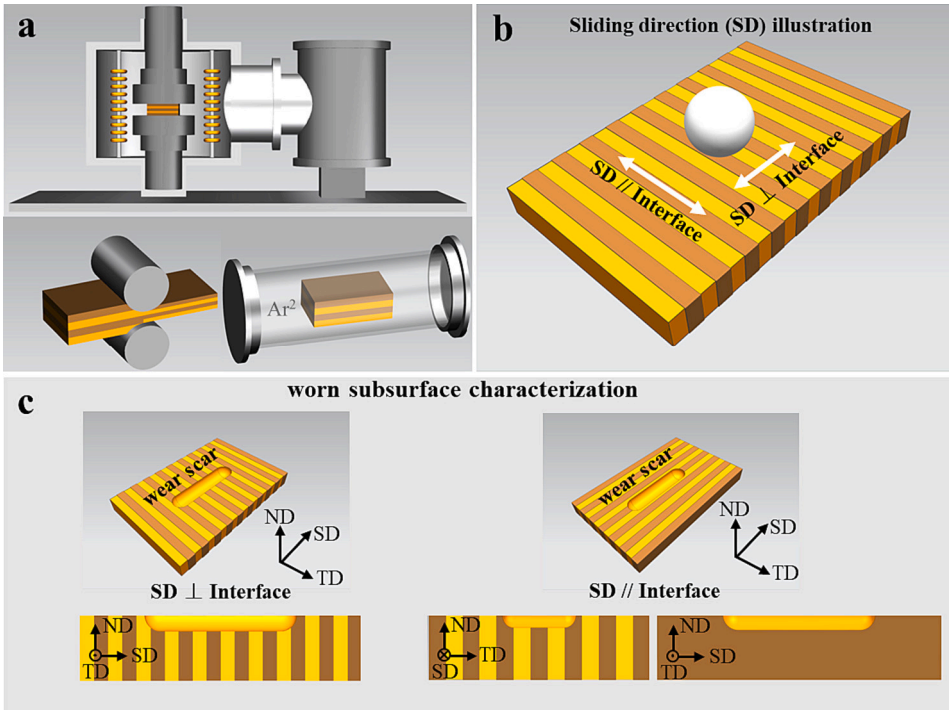


**Fig. 1.** (a) Schematic of the experimental set-ups to fabricate the heterogeneous laminates: diffusion welding, cold-rolling and heat treatment. (b and c) Schematic diagrams of the friction tests (b) and worn subsurface characterization (c). Two sliding directions (SD) were chosen for comparison: one is parallel to the interface and the other one is perpendicular. A frame of reference for the sample coordinate system was defined by the SD, the transverse direction (TD) and the direction normal to the sliding surface (ND). For the sample sliding perpendicular to the interface, the ND-SD cross-sections were prepared. While for the parallel one, both the ND-TD and ND-SD cross-sections were characterized.

mechanically polished with 3.5 μm diamond suspensions (Zhengzhou research institute, China) to remove the native oxide, followed by ultrasonic cleaning in acetone to remove oil. Next, the Cu and CuZn sheets with 1 mm and 0.8 mm thickness respectively were cross-stacked alternately and joined together using diffusion welding at a pressure of 2.5 MPa at 920 °C for 2 h under argon protection. The initial thickness is 36 mm, including 20 layers for each component. Afterwards, the laminate was cold-rolled at room temperature to achieve the desired layer spacing, with each pass resulting in approximately 10% thickness reduction.

In this work, laminates with layer spacing of 20, 50, 100 and 200 μm were prepared, referred to as Laminate-20, Laminate-50, Laminate-100 and Laminate-200 hereinafter. The four laminates were subsequently annealed in a tube furnace at 350 °C for 3 h with argon flow to attain fully recrystallized grains. HMV-705 tester (SHIMADZU, Japan) was used to measure the microhardness of the laminates with a loading duration of 10 s. For each layer, at least ten hardness experiments were performed.

### 2.2. Friction and wear tests

Dry sliding tests of the laminates were performed on a linear reciprocating tribometer (UMT-2, Germany) with a ball-on-plate contact configuration at room temperature. The relative humidity in air was maintained at 35 ± 5%. $Al_2O_3$ balls with 6 mm diameter served as the counter bodies since they are much harder than the Cu/CuZn laminates. Prior to the friction tests, all samples were mechanically polished with 3.5 μm diamond suspensions and then electro-polished in an electrolyte consisting of 90% phosphoric acid and 10% deionized water at room temperature. Two sliding directions, perpendicular and parallel to the interface, were intentionally chosen to explore the friction and wear anisotropy, as schematically shown in Fig. 1b. Sliding loads of 2 N and 5 N, and a sliding speed of 1 mm/s were applied. The sliding cycles were 10, 100 and 900. The sliding stroke was 2 mm. In addition, the Laminate-20 sample was subjected to a high tribological stress by sliding against a 1 mm diameter $Al_2O_3$ ball with a normal load of 2 N. The sliding speed was kept constant and the COF was automatically recorded by the tribometer. To determine the wear volume, 3D profiles of wear scars were measured using a spectral confocal profiler (SM-1000, Applied Scientific Instrumentation, USA). The specific wear rate (K) is calculated by the following expression:

$$K = \frac{W}{FL} \tag{1}$$

Where W is the wear volume which was obtained by the 3D profiler, while F and L represent the normal load and the total sliding distance, respectively.

### 2.3. Wear surface and subsurface microstructure characterization

A scanning electron microscope (SEM, Quanta 250 FEG, USA) equipped with an energy dispersive spectroscopy (EDS) detector was used to examine surface morphologies and elemental distributions at an acceleration voltage of 15 kV. For the laminates sliding perpendicular to the interface, cross-sections were prepared parallel to the sliding direction (Fig. 1c) by wire cutting, ground to the center of the wear scars and electro-polished. For the laminates sliding parallel to the interface, two types of cross-sections were prepared by cutting parallel and perpendicular to the sliding direction, respectively. All cross-sections were examined by electron backscatter diffraction (EBSD) with a focused ion beam/scanning electron microscopy dual-beam system (FIB/SEM, Zeiss Auriga, Germany) at an acceleration voltage of 15 kV. The step size was 100 nm. The EBSD orientation data was analyzed with the Channel 5 software and the Kernel average misorientation (KAM) method was used to measure the local misorientation (θ) with a threshold value of 5°, beyond which the misorientation is interpreted as grain boundaries. The geometrically necessary dislocation (GND) density was estimated by:

$$\rho^{GND} = \frac{2\theta}{ub} \tag{2}$$

where u is the step size (100 nm) and b denotes the length of the Burgers vector (0.255 nm for copper).

Cross-sectional transmission electron microscope (TEM) foils were prepared through a standard FIB lift-out technique from the center of the wear scar, as shown in Fig. 1c. The worn subsurface structures were characterized with a TECNAI $G^2$ 20 TEM with an acceleration voltage of 200 kV. High-resolution scanning TEM (HRSTEM) images were taken using a FEI Titan ChemiSTEM $G^2$ 80–200 TEM at 200 kV.

## 3. Results

### 3.1. Microstructures of the cu/CuZn laminates

The EBSD inverse pole figure (IPF) maps clearly show the interfaces between the Cu and CuZn layers in four different laminates (Figs. 2a-d). Additionally, SEM images and corresponding EDS mappings of these samples indicate well-defined laminate structure (Fig. S1). Taking Laminate-200 as an example, the layer thickness of Cu and CuZn are about 200 ± 20 μm. The cold rolling and subsequent annealing processes led to a pronounced recrystallization in each layer. The grain size of the Cu layer is much larger than that of the CuZn layer.

The grain size and hardness are plotted as a function of the layer spacing for each sample (Figs. 2e and f). In total, 300 grains for the CuZn layer and 100 grains for the Cu layer were measured to obtain their average grain sizes for all the laminates. The average grain sizes in both layers increase with the layer spacing, corresponding to the hardness variation. The hardness of the CuZn layer decreases from 150 to 115 HV with increasing layer spacing, while the hardness of the Cu layer remains around 80 HV, independent of the layer spacing. For each sample, the grain size within the Cu layer varies from a few hundred nanometers to a few microns, whereas the grain size distribution within the CuZn layer is relatively uniform, as depicted in Fig. 2e. Note that the difference in hardness between the Cu and CuZn layers increases as the layer spacing decreases.

### 3.2. Friction and wear anisotropy

To systematically investigate friction anisotropy, the friction and wear of all four laminates with different layer spacings were evaluated in both sliding directions (perpendicular and parallel to the interfaces) while keeping all other variables constant (Figs. 3a-b). When sliding parallel to the interface, the COF slightly decreases and then increases with increasing layer spacing, reaching around 0.45. The COF changes similarly when sliding perpendicular to the interface. The COFs during sliding perpendicular to the interface are lower than those during parallel sliding when the layer thickness is below 50 μm (Fig. 3a). The wear rate also shows strong anisotropy when the layer spacing is below 50 μm. For comparation, the friction properties of pure Cu and CuZn samples fabricated by the same processing parameters as Cu/CuZn laminates are listed in Fig. S2. The COFs increase quickly to a steady value of 0.5 for Cu and 0.4 for CuZn, respectively.

In Laminate-100, the COF reaches a steady state after 400 cycles for both sliding directions and the COF values are almost identical (Fig. 3c). However, for Laminate-50, the COF curves display noticeable friction anisotropy (Fig. 3d). The COF increases to a steady value of 0.45 when sliding parallel to the interface, in analogy to Laminate-100. In contrast, the COF is much lower during sliding perpendicular to the interface. The COF variations of the Laminate-20 and 200 samples with different sliding directions are shown in Fig. S3.

In order to interpret the friction anisotropy, the surface morphology

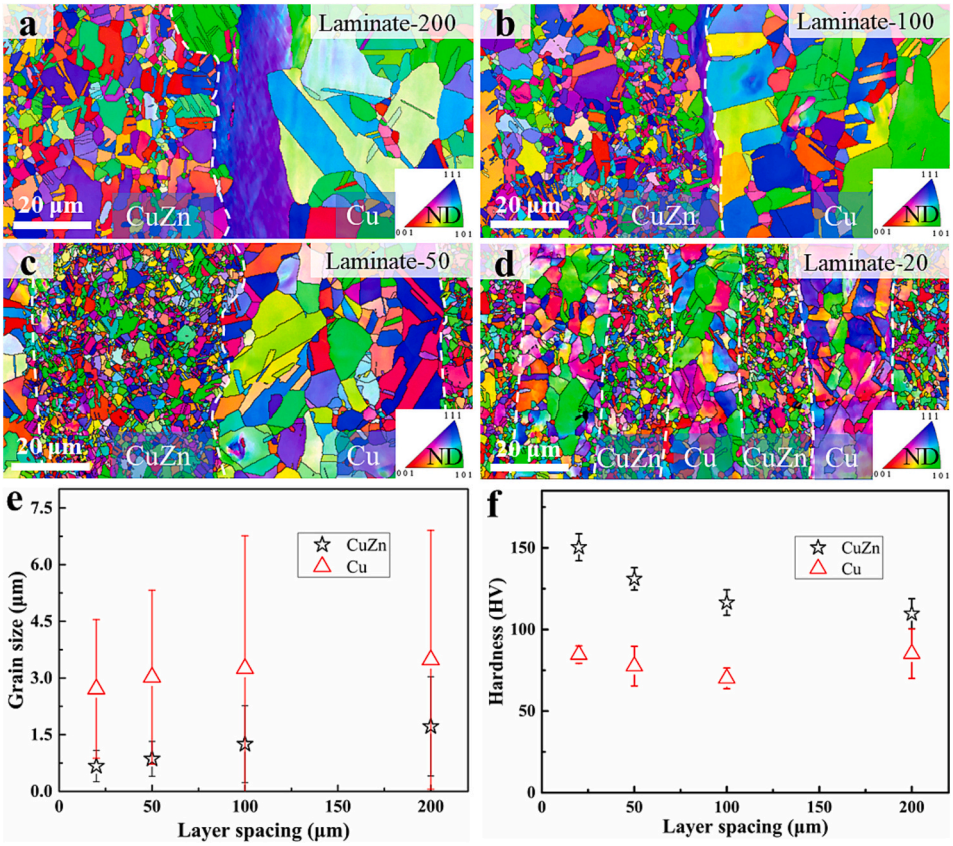


**Fig. 2.** EBSD IPF mappings of the laminates with different layer spacings: (a) 200 μm; (b) 100 μm; (c) 50 μm and (d) 20 μm. They are color coded with respect to ND. (e) Variation of the grain size with the layer spacing. (f) Hardness measurements of the laminates with different layer spacings.

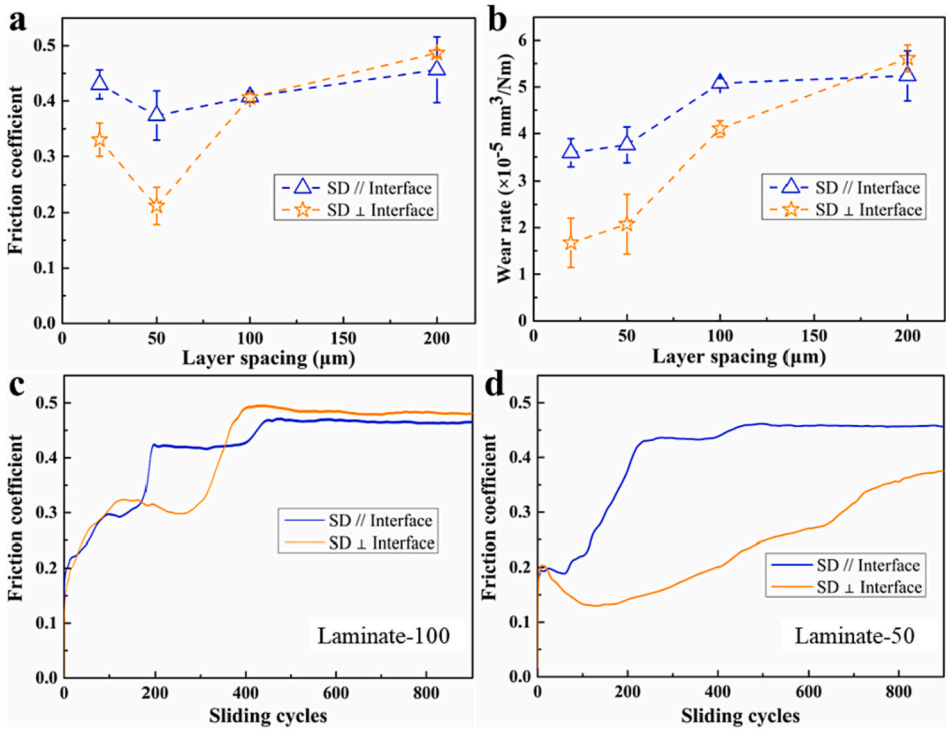


**Fig. 3.** (a-b) Variations of the COF (a) and wear rate (b) with the layer spacing for the laminates sliding perpendicular and parallel to the interface under a normal load of 5 N and sliding cycles of 900. (c-d) COF curves of the samples with layer spacings of 100 μm (c) and 50 μm (d) in different sliding directions. $Al_2O_3$ ball with a diameter of 6 mm was applied.

and elemental distributions were investigated (Fig. 4). The noteworthy feature is that, with the reducing layer spacing, the surface morphological pattern changes from slight vortex-like flow to complete chemical mixing (Figs. 4a-c). For Laminate-200 and Laminate-100, the interface is curved after multiple sliding, but still discernable in the wear scars from the EDS results. In contrast, for Laminate-50, the interface is almost absent in the wear scar (Fig. 4c), indicative of strong chemical mixing between the Cu and CuZn layers. In addition, for Laminate-50 sliding parallel to the interface, little chemical mixing occurs and the interfaces remain straight (see Fig. 4d). Furthermore, enlarged SEM images exhibit different worn morphologies after 900 sliding cycles (Fig. 5a and 6a): the surface remains smooth when sliding perpendicular to the interface, while obvious delamination and peeling-off of the CuZn layer take place in the parallel case (as shown in the element distribution in Fig. S4a).

### 3.3. *Worn subsurface structure*

In order to comprehend the microstructure-dependent friction anisotropy and difference in worn morphologies, cross-sectional EBSD and TEM characterizations of the worn subsurface structure were compared for the Laminate-50 sample (Figs. 5 and 6) for both sliding directions. When sliding perpendicular to the interface, a mixing layer is formed on top of the CuZn layer (Fig. 5b), taken from the area as indicated in Fig. 5a. The EDS results show that the mixing layer consists of Cu with minor Zn content (Figs. S5a and b). The grains are much more refined in the mixing layer (Fig. 5b). Note that the CuZn grains close to the interface are smaller than the ones in the middle regions below the mixing layer. Fig. S5c presents a cumulative distribution plot, indicating abnormal grain coarsening from 3.5 μm to 7.5 μm in the CuZn layer. Large amounts of GNDs exist in both the Cu and CuZn layers within a depth of about 20 μm (Fig. 5c). A cross-sectional TEM image (Fig. 5d) shows that the grains in the topmost mixing layer have different structural features: ultra-fined grains in the topmost area and adjacent nanograins, as evidenced by the selected area electron diffraction (SAED) pattern. The corresponding EDS line scanning along the depth direction of the TEM specimen (Fig. S5d) further shows that the mixing layer consists of Cu with minor Zn content.

For the Laminate-50 sample sliding parallel to the interface, two types of cross-sections were prepared as mentioned earlier: one was along the ND-TD plane (Fig. 6b), and the other one was along the ND-SD plane for both layers (Figs. 6d and f). There is no vortex-like mixing layer, consistent with the previous EDS result (Fig. 4d). The IPF mapping (Fig. 6b) shows that the plastic deformation of CuZn layer is not visible due to the small grain size. The GNDs density and deformation depth in the Cu layer are larger than that in the CuZn layer (Fig. 6c). For the ND-SD cross-sections of both two layers (Figs. 6d-g), the discrepancy is similar for the GNDs. We further prepared a TEM foil from the worn subsurface CuZn layer in Fig. 6d, with FIB extraction direction parallel to the sliding direction. The TEM image (Fig. 6h) of the CuZn layer shows a gradient of grain size distribution from the surface to the bulk interior. The grain size gradually increases to the sub-micron scale with increasing depth. The inset SAED pattern indicates typical friction-induced nanograins in the topmost layer.

In order to elucidate the difference in deformation mechanisms and tribo-induced damage accumulations, the worn surface and subsurface

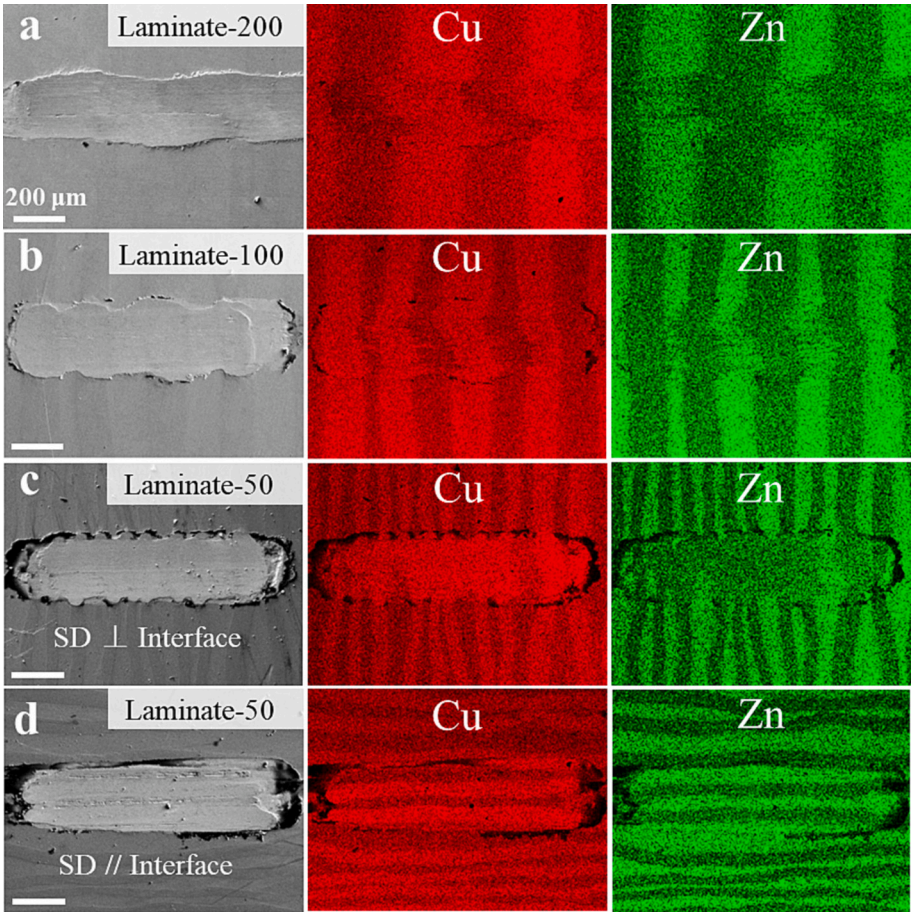


**Fig. 4.** SEM images and corresponding EDS mappings of the wear surfaces of (a) Laminate-200 and (b) Laminate-100 with the sliding direction perpendicular to the interface under a normal load of 5 N after 900 cycles. (c-d) SEM images and EDS mappings of the wear surfaces of Laminate-50 sliding (c) perpendicular and (d) parallel to the interface under a normal load of 5 N after 900 cycles. $Al_2O_3$ ball with a diameter of 6 mm was used.

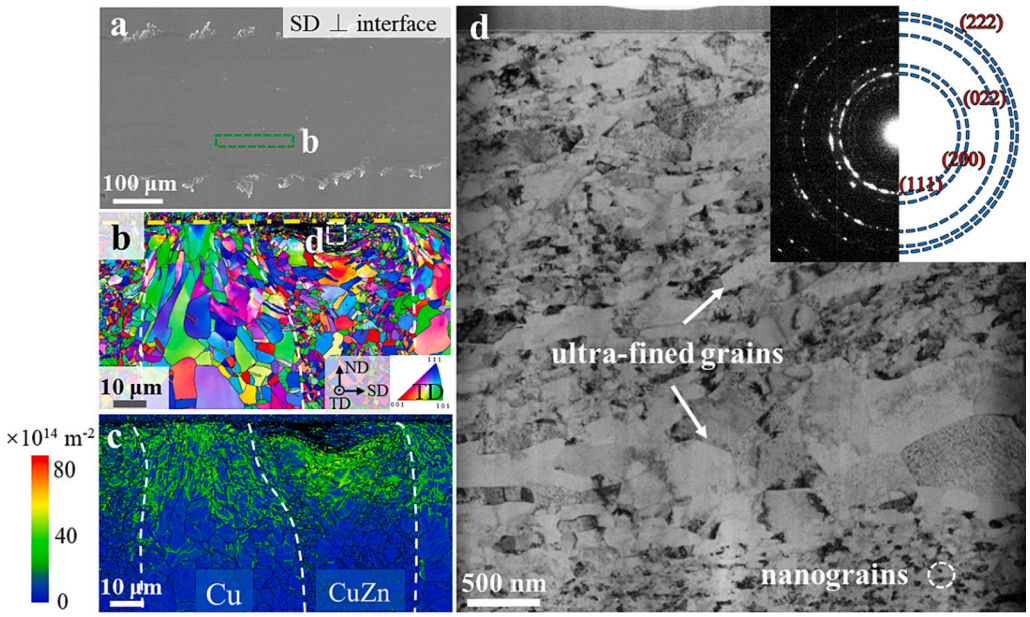


**Fig. 5.** (a) An enlarged SEM image of the surface morphology for the Laminate-50 sample sliding perpendicular to the interface under a normal load of 5 N after 900 cycles. (b) IPF mapping with respect to TD of the worn subsurface structure. The surface is outlined by the yellow dashed line. (c) GND density mapping. The color bar in the GND density mapping means the number of GNDs per unit area. (d) Cross-sectional TEM image of the topmost mixing layer. The inset shows a SAED pattern of the white dashed circle. $Al_2O_3$ ball with a diameter of 6 mm was used. (For interpretation of the references to color in this figure legend, the reader is referred to the web version of this article.)

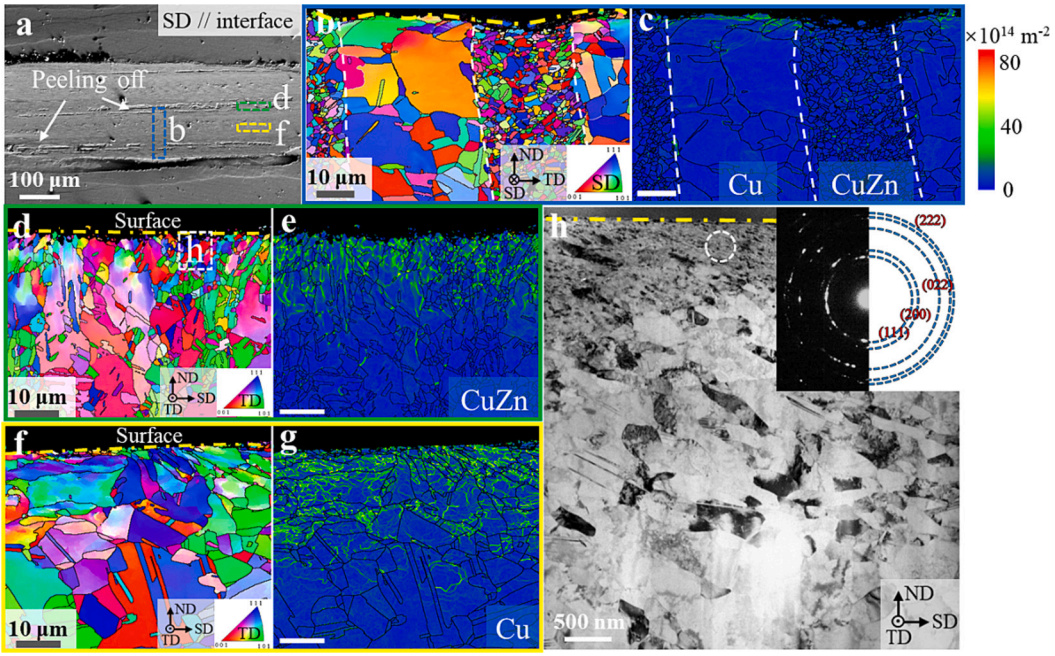


**Fig. 6.** (a) An enlarged SEM image of the surface morphology for the Laminate-50 sample sliding parallel to the interface under a normal load of 5 N after 900 cycles. (b-c) IPF mapping with respect to SD of the ND-TD worn cross-section (b) and corresponding GND density mapping (c). (d-g) IPF mappings with respect to TD (d and f) and corresponding GND density mappings (e and g) of the ND-SD cross-sections for the CuZn and Cu layers. (h) Cross-sectional TEM image of the topmost CuZn layer in (d). The inset shows the SAED pattern of the topmost grains. $Al_2O_3$ ball with a diameter of 6 mm was used.

structure near the interface in the very early stage were compared for the Laminate-50 samples with both sliding directions (Fig. 7). When sliding perpendicular to the interface, only abrasive wear occurs. While in the parallel case, peeling off of the CuZn layer occurs (Fig. 7b and Fig. S4b). The corresponding cross-section (insert in Fig. 7b) confirms that a delaminating tribolayer is formed in the subsurface CuZn layer. Fig. 7c displays the microstructures near the interface for the sample sliding perpendicular to the interface, showing deformation twins and dislocations in the CuZn layer in the vicinity of the interface (Fig. 7e). The SAED pattern suggests a twinning relationship, with the twin thickness estimated to be about 100 nm. In the Cu layer, dislocation slip is the dominating deformation mechanism. In contrast, when sliding parallel to the interface, dislocation-dominated grain refinement is observed in both Cu and CuZn layers (Fig. 7d). By contrast, the CuZn grain close to

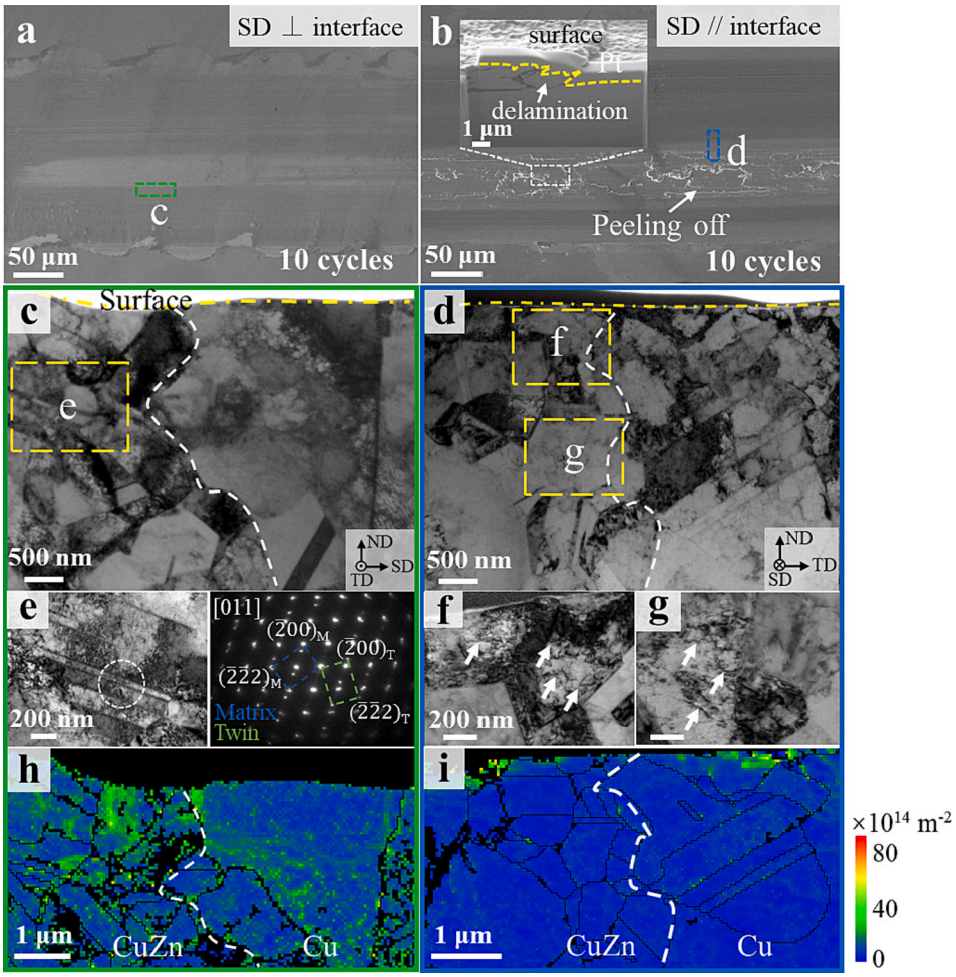


**Fig. 7.** (a-b) SEM images of the worn surfaces for Laminate-50 under both sliding directions after 10 cycles. The insert in (b) shows a delamination layer formed in the CuZn layer. (c and d) TEM images of worn subsurface microstructure near the heterogeneous interface taken from the area in (a) and (b) respectively. (e-g) TEM images taken from the dashed rectangle in (c) and (d), the corresponding selected area electron diffraction (SAED) pattern in (e) is taken from the white dashed circle. The zone axis is [011]. (h-i) Corresponding GND density mappings of (c) and (d) respectively. The color bar in the GND density mapping means the number of GNDs per unit area. A load of 5 N and $Al_2O_3$ ball with a diameter of 6 mm were applied.

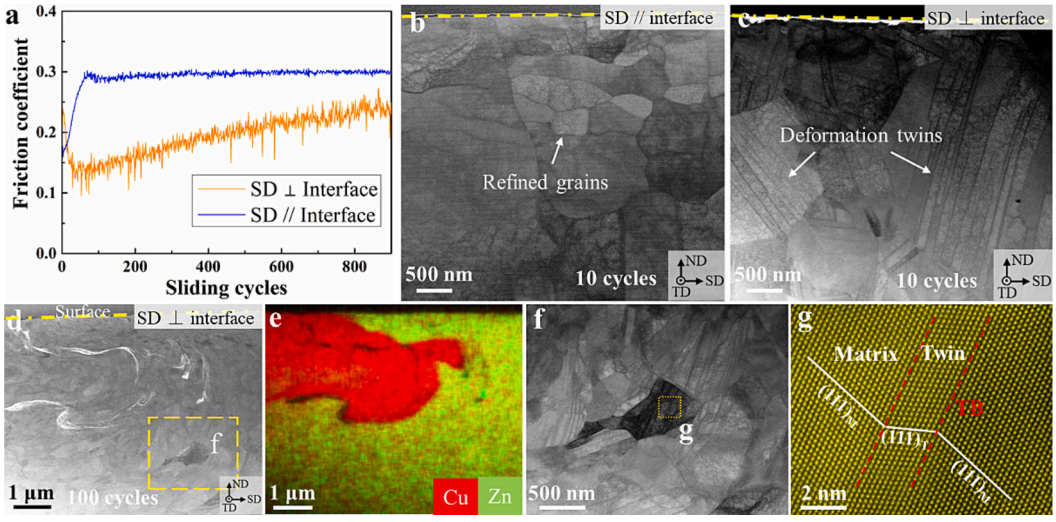


**Fig. 8.** (a) COF curves of the Laminate-20 sample for both sliding directions after 900 cycles. (b-c) Bright field STEM images of the worn subsurface CuZn layer for Laminate-20 under both sliding directions after 10 cycles: (b) parallel to the interface and (c) perpendicular to the interface. (d) Bright field STEM image of the worn subsurface CuZn layer for the Laminate-20 sample sliding perpendicular to the interface after 100 cycles. (e) Corresponding EDX mapping of (d). (f) An enlarged bright field STEM image of the twinned grains in (d). (g) HRSTEM image showing deformation twinning as indicated in (f). The sample coordinate systems are marked in the TEM images. A load of 2 N and $Al_2O_3$ ball with a diameter of 1 mm were applied for each sample.

the interface is composed of dislocations (Figs. 7f-g), as indicated by the white arrows. Figs. 7 h and i show the corresponding GNDs density distributions for Figs. 7c and d, respectively. It is seen that the density of GNDs for the sample sliding perpendicular to the interface are much larger than for the parallel one across the entire deformation regions. In addition, for 100 sliding cycles (Figs. S4c-d), the worn surface morphologies are similar to those for ten cycles under both sliding directions.

### 3.4. Friction anisotropy under different contact pressures

Taking the effect of applied stress on the friction anisotropy into account, additional sliding tests were conducted on some laminates with different contact pressures by adjusting the normal loads and counterbody diameters. The Young's modulus of 110 GPa for Cu and 360 GPa for $Al_2O_3$ and a Poisson ratio of 0.32 for Cu and 0.23 for $Al_2O_3$ were used to calculate the Hertzian contact pressure, respectively.

First, a load of 2 N and 1 mm $Al_2O_3$ balls were selected to attain a Hertzian contact pressure of ~2.37 GPa, 144% higher than the ~0.97 GPa in previous friction tests. The friction anisotropy is again found for the laminate-20 sample (Fig. 8a) under this condition. The COF increases to a steady value of 0.3 when sliding parallel to the interface. In contrast, the COF remains lower and increases slowly in the perpendicular case. Figs. 8b-c show the worn subsurface microstructures of the CuZn layer for both sliding directions after ten sliding cycles. When sliding parallel to the interface (Fig. 8b), grain refinement with a large number of dislocations can be observed within a 2 μm thick layer below the surface. In the perpendicular case (Fig. 8c), a large number of deformation twins accompanied by dislocations are generated below the contact surface, with no significant change in grain size. We further performed the friction test on the Laminate-20 sample after 100 cycles, with the sliding direction perpendicular to the interface. Fig. 8d shows the formation of the mixing layer in the worn subsurface CuZn layer, and the EDS mapping (Fig. 8e) shows that the vortex-like structure is composed of copper and minor Zn content. Many deformation twins exist in the grains below the mixing layer in Fig. 8f. The HRSTEM image reveals the atomic-scale twinning structure (Fig. 8g).

Second, a load of 2 N and 6 mm $Al_2O_3$ balls were selected to attain a low Hertzian contact pressure of ~0.72 GPa. Friction tests were carried out on the Laminate-50 samples under both sliding directions. No friction anisotropy is generated either in the early stage or the steady state (Fig. 9a), with COFs reaching a steady value of 0.5. SEM images of the worn surface (Figs. 9b-c) show identical wear scar width and peeling off of the surface layer for both directions. Cross-sectional worn subsurface microstructures were characterized by EBSD for both directions (Figs. 9d-g). No obvious grain refinement exists in either the Cu or the CuZn layers. The GND density mappings show that the GNDs only exist within a depth of about 10 μm in the topmost Cu layer, with only a few in the CuZn layer for both sliding directions (Figs. 9e and g).

## 4. Discussion

### 4.1. Size effect on chemical mixing in heterogeneous laminates

The principal finding is that friction-induced chemical mixing perpendicular to the interfaces is significantly stimulated with the decreasing layer spacing less than a critical value of 50 μm under a maximum Hertzian contact stress of 0.97 GPa. This can be interpreted from the following two aspects.

First, the applied tribological stress is unable to cause mass transport of soft Cu over the entire CuZn layer, when its spacing is large enough (see Fig. 4). This can be explained by the subsurface in-plane shear stress $\sigma_{xz}$ calculated by the Hamilton's model [44] at a COF of 0.4 for the loads of 2 and 5 N (Fig. 10a and c). The highest shear stress (~380 MPa) at the front of the indenter is at a depth of about 15 μm for the load of 5 N. We then plot the stress distribution along the sliding direction at this depth (Fig. 10b), where x = 0 represents the middle of the indenter. It can be seen that the compressive stress at the front of the indenter increases

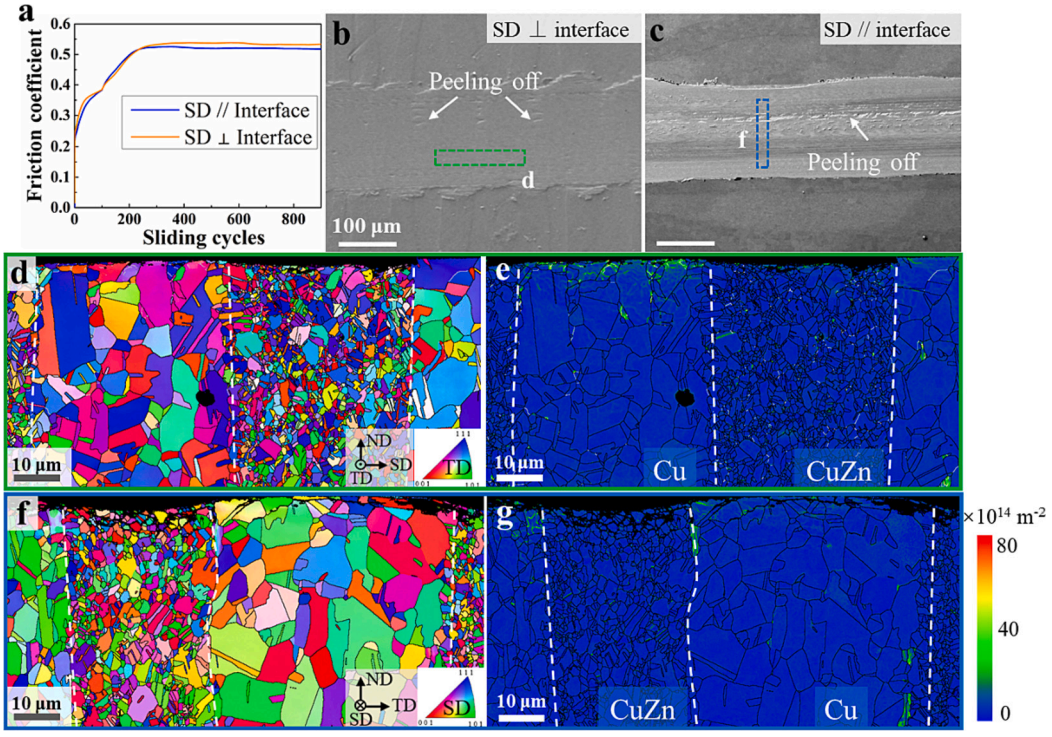


**Fig. 9.** (a) COF curves of Laminate-50 under both sliding directions after 900 cycles. (b-c) SEM images of the worn surfaces for each direction. (d-g) IPF mappings (d and f) and corresponding GND density mappings (e and g) of the worn subsurface layer for both sliding directions: (d and e) perpendicular to the interface; (f and g) parallel to the interface. The sample coordinate systems are marked, and the IPF mappings are color coded with respect to TD and SD, respectively. The color bar in the GND density mapping means the number of GNDs per unit area. A load of 2 N and $Al_2O_3$ ball with a diameter of 6 mm were applied.

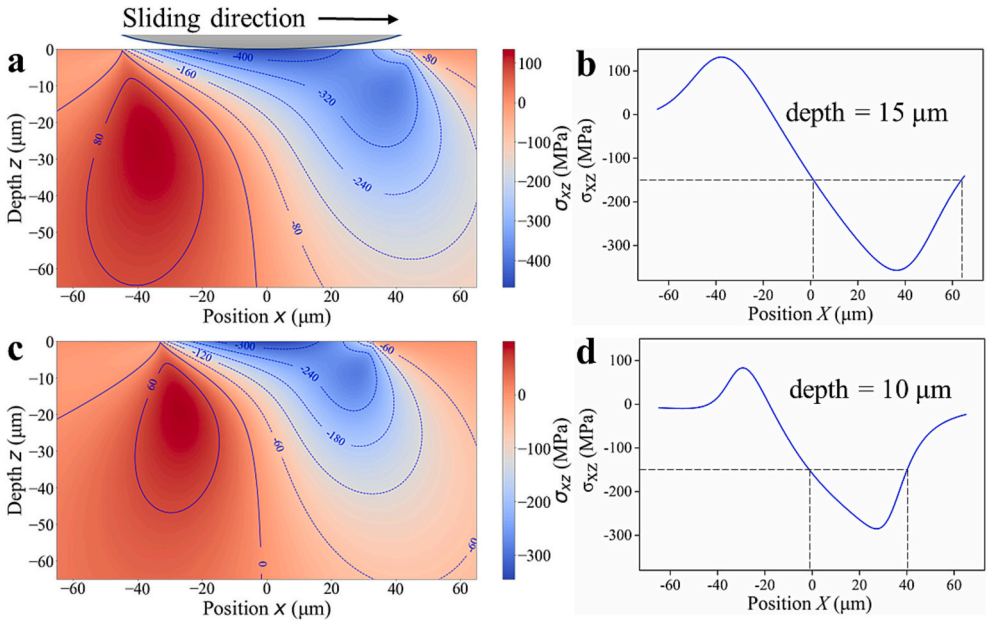


**Fig. 10.** The xz component of the stress field along the sliding direction at a COF of 0.4 under normal loads of 5 N (a) and 2 N (c), and the lines indicate the contours of constant stress. Variation of applied shear stress along the x-axis at a depth of 15 μm (b) for 5 N and 10 μm (d) for 2 N. $Al_2O_3$ ball with a diameter of 6 mm was used.

first and then decreases with increasing distance. The maximum width of the stress field exceeding the yield strength of Cu (150 MPa) is about 60 μm, which is larger than the layer spacing in the Laminate-50 sample with substantial mixing. This means that the different layers can deform concurrently in response to large tribological strains in the Laminate-50 sample. However, with decreasing tribological stress, no friction anisotropy and significant chemical mixing are observed for the same laminate. Figs. 10c-d show the shear stress component $\sigma_{xz}$ under a load of 2 N. At the depth (~ 10 μm) with the maximum shear stress at the front of indenter, the width exceeding the yield strength is determined to

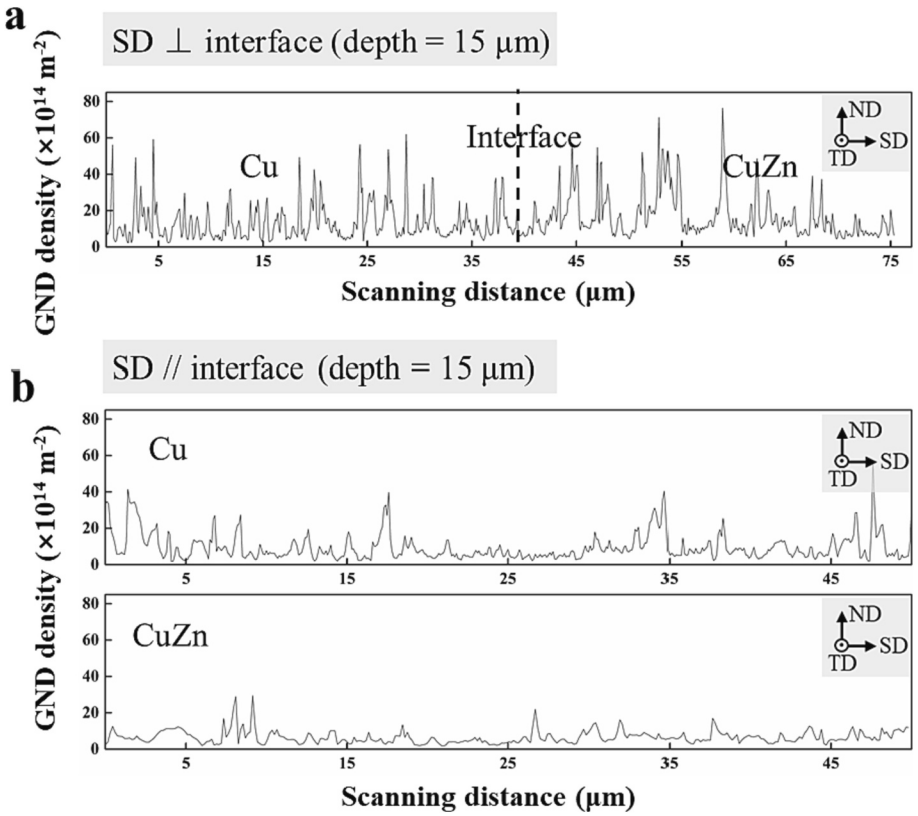


**Fig. 11.** Variation of the GND density along the sliding direction at a depth of 15 μm for Laminate-50 under both sliding directions after 900 cycles: (a) perpendicular to the interface and (b) parallel to the interface. The upper and lower curves in (b) refer to the Cu and CuZn layer, respectively. A load of 5 N and $Al_2O_3$ ball with a diameter of 6 mm were applied.

be about 40 μm (Fig. 10d), which is less than the laminate layer spacing. This is further supported by the stress field analysis of the Laminate-20 sample with chemical mixing when sliding against a 1 mm $Al_2O_3$ ball under 2 N (Fig. S6), where the maximum shear stress width in front of the indenter exceeding the yield strength is about 35 μm (Fig. S6b). Overall, the above stress field analysis indicates that the matching of the applied shear stress and the layer spacing is the decisive factor in triggering significant chemical mixing.

Second, the dislocation activity across the heterogeneous interfaces is supposed to facilitate chemical mixing. This proposition is supported by the calculated distributions of GNDs in the worn subsurface layer for the Laminate-50 sample under both sliding directions after 900 cycles (see Figs. 5c and 6c). The GNDs density for the sample sliding perpendicular to the interface is noticeably larger than that parallel to the interface. A thick surface layer with many GNDs is to accommodate a large strain gradient in both Cu and CuZn layers when sliding perpendicular to the interface. While for the other direction, a much smaller gradient is generated in the Cu and CuZn layers (Fig. 6c). The GNDs distributions along the sliding directions at a depth of 15 μm were further compared (Fig. 11) for both directions. For the perpendicular case (Fig. 11a) plotted from Fig. 5c, the GNDs distribution within the Cu layer is relatively uniform, while there is a concentration of GNDs in the middle region of the CuZn layer. Fig. 11b shows the GNDs distribution within both layers when the sliding direction is parallel to the interface, plotted from Figs. 6e and g. The GNDs distribution is relatively uniform, and the values are smaller than those for sliding perpendicular to the interface. The higher GNDs density is expected to facilitate the forced chemical mixing. It is postulated that the dispersive GNDs distribution along the sliding direction will again suppress the strain localization, which is favorable for chemical mixing between the laminates under multiple sliding. The detailed deformation mechanisms will be discussed later.

In the early stage prior to chemical mixing between the laminates, a high density of twins and dislocations in the CuZn layer releases the strain concentration near the interfaces (Fig. 7c). The heterogeneous interfaces are deduced to be responsible for chemical mixing during multiple sliding, on the basis of strain delocalization along both the depth and sliding direction. It is expected that greater interfacial dislocation plasticity will result in less strain localization, leading to enhanced chemical mixing between the soft and hard laminates.

### 4.2. Subsurface deformation mechanisms with heterogeneous interfaces

When sliding parallel to the interfaces, a delaminating tribolayer forms in the CuZn layer (Figs. 6a and 7b), which is consistent with previous studies on wear mechanisms of Cu alloys and Cu matrix composites [22,45–48]. This is due to the concentration of large plastic strains and strain gradients in the topmost layer, leading to the cracking and peeling-off of the tribolayer (Fig. 7b). The subsurface stress field analysis reveals that the shear stress component $\sigma_{xz}$ has a gradient distribution from the top surface (~450 MPa) to the bulk interior right below the indenter (Fig. 10a). The topmost layer (~5 μm in thickness) experiences very high stresses that exceed the yield stress of Cu and CuZn, leading to the formation of a delaminating tribolayer and a high COF.

In contrast, when sliding perpendicular to the interfaces, the surface remains smooth for all sliding cycles (Figs. 5a and 7a). The confinement of heterogeneous interfaces effectively promotes the synergistic deformation of the two layers, mitigating the formation of the brittle tribolayer. At the very beginning of sliding for the samples demonstrating frictional anisotropy, many deformation twins accompanied by some dislocations occur in the CuZn layer when sliding perpendicular to the interface. The formation of a delaminating tribolayer is significantly retarded. In contrast to tensile deformation of Cu/CuZn laminates [27,49], both the soft Cu and hard CuZn domains deform simultaneously under tribological loading in the very early stage of sliding. The tensile deformation of the CuZn layer is dominated by GND pile-ups when the tensile strain is typically less than 0.3 [27]. While for multiple sliding with large strains, a large number of deformation twins are formed in the CuZn layer when sliding perpendicular to the interface.

### 4.3. Origins of friction anisotropy

With strong evidence for the existence or in some cases nonexistence of friction anisotropy, our study points out that friction anisotropy is ultimately related to the laminate layer spacing and the applied tribological shear stress. Friction anisotropy is activated when the layer spacing is less than a critical value (~50 μm) for a constant tribological stress (~ 0.97 GPa). In other words, friction anisotropy is triggered when the tribological stress is higher than a critical value for a certain laminate. We calculated the minimum contact stress required to trigger friction anisotropy for samples with varying layer spacings, as schematically illustrated in Fig. 12 (dashed blue line). Smaller layer spacing and higher tribological stress are expected to trigger friction anisotropy in the heterogenous laminates. In anisotropic conditions, the friction and wear during perpendicular sliding are lower than those during sliding parallel to the laminate interface.

Friction anisotropy is largely related to strain delocalization not only along the depth but also across the interfaces. First, sliding perpendicular to the interfaces brings about many CuZn deformation twins in the vicinity of the interfaces, in contrast to the parallel case (the insets in Fig. 12). The twinning discrepancy is more pronounced when the tribological stress is significantly elevated from 0.97 to 2.37 GPa. In addition to GNDs pile-up, the twins contribute to the strain gradients across the interfaces and thus suppress the strain localization in the CuZn layer. Similar dislocations activity and grain refinement are activated in the Cu layers for both sliding directions. Second, friction-induced chemical mixing perpendicular to the interfaces is significantly stimulated below the critical layer spacing, mitigating the formation of a delaminating tribolayer. As supported by the experimental results and stress field analysis, the tribological strain is mainly confined in the topmost layer with a large strain gradient along the depth during parallel sliding, leading to strain localization and the formation of a delaminating tribolayer (Figs. 6a and 7b). In contrast, a much smaller strain gradient is present when sliding perpendicular to the interfaces. Taken as a whole, the outstanding tribological properties of heterogeneous laminates are primarily attributed to interface-induced strain delocalization.

## 5. Conclusions

Bulk heterogeneous coarse-grained Cu/CuZn laminates with different layer spacings (20–200 μm) were fabricated by diffusion welding, cold rolling and subsequent heat treatment, wherein the grain size of the Cu layer is much larger than the CuZn layer. The effect of layer spacing on the tribological properties and corresponding friction anisotropy were systematically investigated and linked to surface deformation mechanisms in proximity to the interfaces between the two laminate constituents. Two sliding directions (perpendicular and parallel to the interfaces) were chosen under different tribological shear stresses. The following conclusions can be drawn:

(1) Both the COF and wear rate decrease with the decreasing layer spacing for both perpendicular and parallel sliding directions with respect to the interface of the laminates. Pronounced friction anisotropy occurs below a critical spacing value or above a tribological stress threshold, where the COF and wear rate during perpendicular sliding are much lower than those during sliding parallel to the laminate interface.
(2) In the early stages of sliding and for the samples showing friction anisotropy, sliding perpendicular to the interface leads to a large number of dislocations and deformation twins in the CuZn layer,

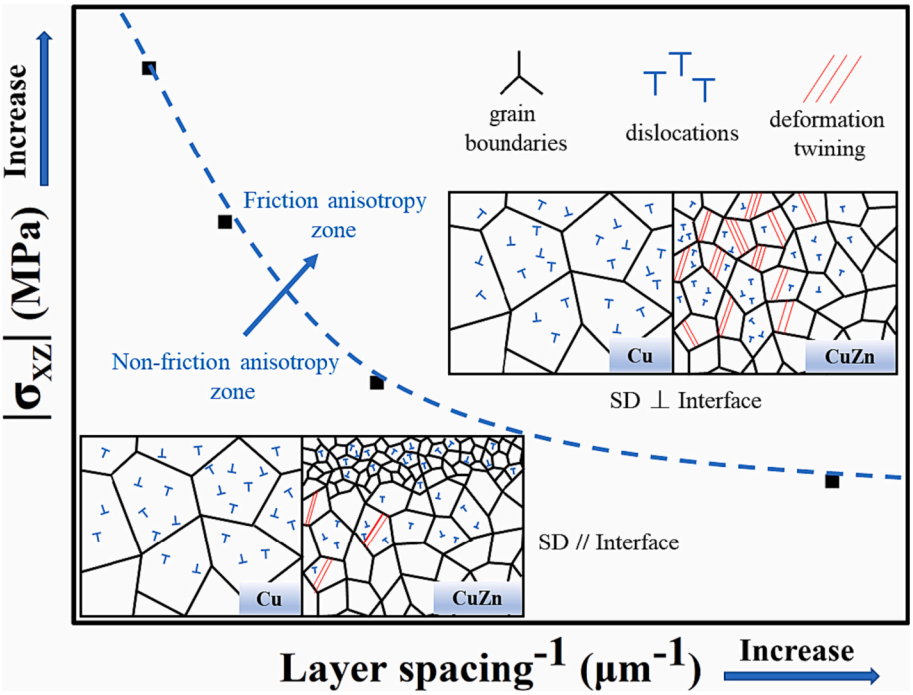


**Fig. 12.** Schematic variations of the tribological shear stress with the inverse of the layer spacing for the existence or nonexistence of the friction anisotropy. The insets depict the surface deformation mechanisms in the early stage for both sliding directions.

in contrast to parallel sliding where few dislocations and twins were detected. This difference in the tendency to deform by twinning is more pronounced when the tribological stress is significantly elevated by 144%. In addition to GND pile-ups, the twins accommodate the tribological strain across the interfaces and suppress strain localization in the CuZn layer.

(3) When sliding parallel to the interfaces between the laminates, the formation of a brittle nanostructured tribolayer dominates in the CuZn layer. When sliding perpendicular to the heterogeneous interface, the dislocation activity across the heterogeneous interfaces is expected to facilitate chemical mixing, mitigating the formation of a delaminating tribolayer. These results ignite the untapped potential in designing heterogeneous laminates with improved tribological properties through rational interface-induced strain delocalization.

## CRediT authorship contribution statement

**Qicheng Zhang:** Writing – original draft, Methodology, Investigation. **Fei Liang:** Methodology, Funding acquisition. **Zhongchen Zhou:** Investigation, Conceptualization. **Yusheng Li:** Investigation. **Julia Rau:** Writing – review & editing, Validation. **Christian Greiner:** Writing – review & editing, Funding acquisition. **Yonghao Zhao:** Writing – review & editing, Methodology. **Yuntian Zhu:** Writing – review & editing, Funding acquisition. **Xiang Chen:** Writing – review & editing, Methodology, Funding acquisition.

## Declaration of competing interest

The authors declare that they have no known competing financial interests or personal relationships that could have appeared to influence the work reported in this paper.

## Data availability

Data will be made available on request.

## Acknowledgements

X. Chen would like to acknowledge financial supports from National Natural Science Foundation of China (Grant No. 92366201, 52371068, 52001165 and 52071180) and the Fundamental Research Funds for the Central Universities (Grant No. 30921011215 and 30922010401). F. Liang acknowledges financial supports from the Jiangsu Funding Program for Excellent Postdoctoral Talent (2022ZB2251). C. Greiner would like to acknowledge funding which has been provided by the European Research Council under ERC Grant Agreement No. 771237, TriboKey. Y. T. Zhu is supported by the Hong Kong Research Grants Council (GRF 11214121). The authors are thankful for the technical support from Jiangsu Key Laboratory of Advanced Micro&Nano Materials and Technology, and the Materials Characterization Facility of Nanjing University of Science and Technology.

## References

[1] W.G. Sawyer, N. Argibay, D.L. Burris, B.A. Krick, Mechanistic studies in friction and wear of bulk materials, Annu. Rev. Mater. Res. 44 (1) (2014) 395–427, https://doi.org/10.1146/annurev-matsci-070813-113533.

[2] T.J. Rupert, C.A. Schuh, Sliding wear of nanocrystalline Ni–W: structural evolution and the apparent breakdown of Archard scaling, Acta Mater. 58 (12) (2010) 4137–4148, https://doi.org/10.1016/j.actamat.2010.04.005.

[3] S.V. Prasad, C.C. Battaile, P.G. Kotula, Friction transitions in nanocrystalline nickel, Scr. Mater. 64 (8) (2011) 729–732, https://doi.org/10.1016/j.scriptamat.2010.12.027.

[4] H.A. Padilla, B.L. Boyce, C.C. Battaile, S.V. Prasad, Frictional performance and near-surface evolution of nanocrystalline Ni–Fe as governed by contact stress and sliding velocity, Wear 297 (1–2) (2013) 860–871, https://doi.org/10.1016/j.wear.2012.10.018.

[5] N. Argibay, T.A. Furnish, B.L. Boyce, B.G. Clark, M. Chandross, Stress-dependent grain size evolution of nanocrystalline Ni-W and its impact on friction behavior, Scr. Mater. 123 (2016) 26–29, https://doi.org/10.1016/j.scriptamat.2016.05.009.

[6] J.F. Curry, T.F. Babuska, T.A. Furnish, P. Lu, D.P. Adams, A.B. Kustas, B.L. Nation, M.T. Dugger, M. Chandross, B.G. Clark, B.L. Boyce, C.A. Schuh, N. Argibay,

Achieving ultralow wear with stable nanocrystalline metals, Adv. Mater. 30 (32) (2018) e1802026, https://doi.org/10.1002/adma.201802026.
[7] J. Xie, J. Yan, D. Zhu, G. He, Atomic-level insight into the formation of subsurface dislocation layer and its effect on mechanical properties during ultrafast laser Micro/Nano fabrication, Adv. Funct. Mater. 32 (15) (2021), https://doi.org/10.1002/adfm.202108802.
[8] A. Rosenkranz, H.L. Costa, M.Z. Baykara, A. Martini, Synergetic effects of surface texturing and solid lubricants to tailor friction and wear – a review, Tribol. Int. 155 (2021), https://doi.org/10.1016/j.triboint.2020.106792.
[9] S. Yuan, N. Lin, W. Wang, H. Zhang, Z. Liu, Y. Yu, Q. Zeng, Y. Wu, Correlation between surface textural parameter and tribological behaviour of four metal materials with laser surface texturing (LST), Appl. Surf. Sci. 583 (2022), https://doi.org/10.1016/j.apsusc.2021.152410.
[10] J. Wang, W. Xue, S. Gao, S. Li, D. Duan, Effect of groove surface texture on the fretting wear of Ti–6Al–4V alloy, Wear 486-487 (2021), https://doi.org/10.1016/j.wear.2021.204079.
[11] J. Huang, S. Yang, Investigation on anisotropic tribological properties of superhydrophobic/superlipophilic lead bronze surface textured by femtosecond laser, Appl. Surf. Sci. 579 (2022), https://doi.org/10.1016/j.apsusc.2021.152223.
[12] S. Qu, J. Wang, X. Hu, F. Lai, Y. Deng, X. Li, Effect of ultrasonic nanocrystalline surface modification process on fretting wear behavior of laser surface textured 20CrMoH steel, Surf. Coat. Technol. 427 (2021), https://doi.org/10.1016/j.surfcoat.2021.127827.
[13] H. Wang, A. Sun, X. Qi, Y. Dong, B. Fan, Wear properties of textured lubricant films filled with graphite and polytetrafluoroethylene (PTFE) via laser surface texturing (LST), Tribol. Int. 167 (2022), https://doi.org/10.1016/j.triboint.2021.107414.
[14] G. Lu, X. Shi, J. Zhang, H. Zhou, Y. Xue, A.M.M. Ibrahim, Effects of surface composite structure with micro-grooves and Sn-ag-cu on reducing friction and wear of Ni3Al alloys, Surf. Coat. Technol. 387 (2020), https://doi.org/10.1016/j.surfcoat.2020.125540.
[15] J. Huang, Y. Guan, S. Ramakrishna, Tribological behavior of femtosecond laser-textured leaded brass, Tribol. Int. 162 (2021), https://doi.org/10.1016/j.triboint.2021.107115.
[16] Z. Wang, Y. Li, F. Bai, C. Wang, Q. Zhao, Angle-dependent lubricated tribological properties of stainless steel by femtosecond laser surface texturing, Opt. Laser Technol. 81 (2016) 60–66, https://doi.org/10.1016/j.optlastec.2016.01.034.
[17] T. Fang, W. Li, N. Tao, K. Lu, Revealing extraordinary intrinsic tensile plasticity in gradient nano-grained copper, Science 331 (6024) (2011) 1587–1590, https://doi.org/10.1126/science.1200177.
[18] F. Liang, X. Xu, P. Wang, Y. Zhang, Z. Han, X. Chen, Microstructural origin of high scratch resistance in a gradient nanograined 316L stainless steel, Scr. Mater. 220 (2022), https://doi.org/10.1016/j.scriptamat.2022.114895.
[19] J. Luo, W. Sun, D. Liang, K. Chan, X. Yang, F. Ren, Superior wear resistance in a TaMoNb compositionally complex alloy film via in-situ formation of the amorphous-crystalline nanocomposite layer and gradient nanostructure, Acta Mater. 243 (2023), https://doi.org/10.1016/j.actamat.2022.118503.
[20] X. Chen, Z. Han, X. Li, K. Lu, Friction of stable gradient nano-grained metals, Scr. Mater. 185 (2020) 82–87, https://doi.org/10.1016/j.scriptamat.2020.04.041.
[21] X. Chen, Z. Han, K. Lu, Friction and Wear reduction in copper with a gradient Nano-grained surface layer, ACS Appl. Mater. Interfaces 10 (16) (2018) 13829–13838, https://doi.org/10.1021/acsami.8b01205.
[22] X. Chen, Z. Han, X. Li, K. Lu, Lowering coefficient of friction in cu alloys with stable gradient nanostructures, Sci. Adv. 2 (12) (2016) e1601942, https://doi.org/10.1126/sciadv.1601942.
[23] X. Xue, Y. Wu, N. Su, X. Heng, Q. Deng, Z. Chang, L. Peng, High-strength GWZ1031K alloy with gradient structure induced by surface mechanical attrition treatment, Mater. Charact. 170 (2020), https://doi.org/10.1016/j.matchar.2020.110701.
[24] X. Wu, M. Yang, F. Yuan, G. Wu, Y. Wei, X. Huang, Y. Zhu, Heterogeneous lamella structure unites ultrafine-grain strength with coarse-grain ductility, Proc. Natl. Acad. Sci. U. S. A. 112 (47) (2015) 14501–14505, https://doi.org/10.1073/pnas.1517193112.
[25] X. Wu, Y. Zhu, Heterogeneous materials: a new class of materials with unprecedented mechanical properties, Mater. Res. Lett. 5 (8) (2017) 527–532, https://doi.org/10.1080/21663831.2017.1343208.
[26] X. Ma, C. Huang, J. Moering, M. Ruppert, H.W. Höppel, M. Göken, J. Narayan, Y. Zhu, Mechanical properties of copper/bronze laminates: role of interfaces, Acta Mater. 116 (2016) 43–52, https://doi.org/10.1016/j.actamat.2016.06.023.
[27] C. Huang, Y. Wang, X. Ma, S. Yin, H.W. Höppel, M. Göken, X. Wu, H. Gao, Y. Zhu, Interface affected zone for optimal strength and ductility in heterogeneous laminate, Mater. Today 21 (7) (2018) 713–719, https://doi.org/10.1016/j.mattod.2018.03.006.
[28] Z. Cao, Z. Cheng, W. Xu, L. Lu, Effect of work hardening discrepancy on strengthening of laminated cu/CuZn alloys, J. Mater. Sci. Technol. 103 (2022) 67–72, https://doi.org/10.1016/j.jmst.2021.06.043.
[29] Y. Wang, Y. Wei, Z. Zhao, Z. Lin, F. Guo, Q. Cheng, C. Huang, Y. Zhu, Mechanical response of the constrained nanostructured layer in heterogeneous laminate, Scr. Mater. 207 (2022), https://doi.org/10.1016/j.scriptamat.2021.114310.
[30] B. Han, J. Huang, Y. Zhu, E.J. Lavernia, Strain rate dependence of properties of cryomilled bimodal 5083 Al alloys, Acta Mater. 54 (11) (2006) 3015–3024, https://doi.org/10.1016/j.actamat.2006.02.045.
[31] H.K. Park, K. Ameyama, J. Yoo, H. Hwang, H.S. Kim, Additional hardening in harmonic structured materials by strain partitioning and back stress, Mater. Res. Lett. 6 (5) (2018) 261–267, https://doi.org/10.1080/21663831.2018.1439115.
[32] S.K. Vajpai, M. Ota, Z. Zhang, K. Ameyama, Three-dimensionally gradient harmonic structure design: an integrated approach for high performance structural materials, Mater. Res. Lett. 4 (4) (2016) 191–197, https://doi.org/10.1080/21663831.2016.1218965.
[33] Y. Zhu, X. Wu, Heterostructured materials, Prog. Mater. Sci. 131 (2023), https://doi.org/10.1016/j.pmatsci.2022.101019.
[34] E. Cihan, H. Stormer, H. Leiste, M. Stuber, M. Dienwiebel, Low friction of metallic multilayers by formation of a shear-induced alloy, Sci. Rep. 9 (1) (2019) 9480, https://doi.org/10.1038/s41598-019-45734-7.
[35] S.K. Ghosh, P.K. Limaye, B.P. Swain, N.L. Soni, R.G. Agrawal, R.O. Dusane, A. K. Grover, Tribological behaviour and residual stress of electrodeposited Ni/cu multilayer films on stainless steel substrate, Surf. Coat. Technol. 201 (8) (2007) 4609–4618, https://doi.org/10.1016/j.surfcoat.2006.09.314.
[36] Z. Luo, G. Zhang, R. Schwaiger, Microstructural vortex formation during cyclic sliding of cu/au multilayers, Scr. Mater. 107 (2015) 67–70, https://doi.org/10.1016/j.scriptamat.2015.05.022.
[37] A. Gola, R. Schwaiger, P. Gumbsch, L. Pastewka, Pattern formation during deformation of metallic nanolaminates, Phys. Rev. Mater. 4 (1) (2020), https://doi.org/10.1103/PhysRevMaterials.4.013603.
[38] X. Ma, B. Gwalani, J. Tao, M. Efe, M. Olszta, M. Song, S. Yadav, A. Yu, T.J. Nizolek, J.S. Carpenter, B. Zhou, A. Devaraj, S. Mathaudhu, A. Rohatgi, Shear strain gradient in cu/Nb nanolaminates: strain accommodation and chemical mixing, Acta Mater. 234 (2022), https://doi.org/10.1016/j.actamat.2022.117986.
[39] D. Luo, Q. Zhou, W. Ye, Y. Ren, C. Greiner, Y. He, H. Wang, Design and characterization of self-lubricating refractory high entropy alloy-based multilayered films, ACS Appl. Mater. Interfaces 13 (46) (2021) 55712–55725, https://doi.org/10.1021/acsami.1c16949.
[40] Y. Wang, J. Li, J. Li, S. Chen, On the strain delocalization mechanism of cu/Nb nanolayered composites with amorphous interfacial layers, Int. J. Plast. 172 (2024), https://doi.org/10.1016/j.ijplas.2023.103856.
[41] C. Yang, C. Yin, Y. Wu, Q. Zhou, X. Liu, Atomic insights into the deformation mechanism of an amorphous wrapped nanolamellar heterostructure and its effect on self-lubrication, J. Mater. Res. Technol. 26 (2023) 4206–4218, https://doi.org/10.1016/j.jmrt.2023.08.215.
[42] M. Dong, Y. Zhu, J. Duan, C. Wang, W. Guo, J. Li, L. Wang, Understanding wear mechanisms of TiSiCN/Zr(C)N coatings at elevated temperatures, Mater. Charact. 180 (2021), https://doi.org/10.1016/j.matchar.2021.111411.
[43] M. Dong, Y. Zhu, J. Li, Effect of amorphous phases induced by friction on wear resistance for TaN/ZrN coatings in thermal oxygen environment, Mater. Charact. 198 (2023), https://doi.org/10.1016/j.matchar.2023.112745.
[44] G.M. Hamilton, Explicit equations for the stresses beneath a sliding spherical contact, Proc. Inst. Mech. Eng. 197 (1983) 53–59.
[45] X. Chen, R. Schneider, P. Gumbsch, C. Greiner, Microstructure evolution and deformation mechanisms during high rate and cryogenic sliding of copper, Acta Mater. 161 (2018) 138–149, https://doi.org/10.1016/j.actamat.2018.09.016.
[46] C. Greiner, Z. Liu, L. Strassberger, P. Gumbsch, Sequence of stages in the microstructure evolution in copper under mild reciprocating Tribological loading, ACS Appl. Mater. Interfaces 8 (24) (2016) 15809–15819, https://doi.org/10.1021/acsami.6b04035.
[47] S. Laube, A. Kauffmann, F. Ruebeling, J. Freudenberger, M. Heilmaier, C. Greiner, Solid solution strengthening and deformation behavior of single-phase cu-base alloys under tribological load, Acta Mater. 185 (2020) 300–308, https://doi.org/10.1016/j.actamat.2019.12.005.
[48] G. Lin, Y. Peng, Y. Li, H.G. Liang, Z. Dong, Y. Zhou, Z. Yue, J. Zhang, D. Xiong, D. Zhang, Remarkable anisotropic wear resistance with 100-fold discrepancy in a copper matrix laminated composite with only 0.2 vol% graphene, Acta Mater. 215 (2021), https://doi.org/10.1016/j.actamat.2021.117092.
[49] J. Zhao, M. Zaiser, X. Lu, B. Zhang, C. Huang, G. Kang, X. Zhang, Size-dependent plasticity of hetero-structured laminates: a constitutive model considering deformation heterogeneities, Int. J. Plast. 145 (2021), https://doi.org/10.1016/j.ijplas.2021.103063.